Mechanical Properties and Applications of Two-Dimensional Materials

Rui Zhang and Rebecca Cheung

Additional information is available at the end of the chapter

Abstract

Two-dimensional (2D) materials have attracted increasing attention recently due to their extraordinarily different material properties compared with conventional bulk materials. The 2D materials possess ultralow weight, high Young's modulus, high strength, outstanding carrier mobility, as well as high anisotropy between the in-plane and out-of-plane mechanical properties. The nearby atoms in the same plane of layered 2D materials are connected via covalent bonding, while the interlayers are stacked together via weak van der Waals interactions. In this article, we review the in-plane mechanical properties (including the in-plane Young's modulus, pretension, breaking strength/strain) and out-of-plane mechanical properties (including the perpendicular-to-plane Young's modulus, shear force constant, and shear strength) of different 2D materials, varying from conductors, semiconductors, to insulators. The different fabrication methods for suspended 2D material structures are presented. The experimental methods and principles for mechanical properties characterization are reviewed. A comparison of the mechanical properties among different 2D materials is summarized. Furthermore, electrical output change as a result of mechanical deformation (piezoresistive and piezoelectric effects) is introduced briefly. By exploiting the unique mechanical and mechanoelectric transduction properties, 2D materials can be used in wide-ranging applications, including flexible electronics, strain sensors, nanogenerators, and innovative nanoelectromechanical systems (NEMS).

Keywords: 2D materials, mechanical properties, suspended structure, strain sensors, nanoelectromechanical systems (NEMS)

1. Introduction

AQ1

1   Since the first successful preparation of graphene by mechanical exfoliation from graphite
2   crystals in 2004 [1], two-dimensional (2D) materials have attracted dramatic attention due to
3   their extraordinary physical properties (ultralow weight, high Young's modulus, and high
4   strength) [2–7] and outstanding electrical properties [1] compared with conventional bulk
5   materials. In the past few years, graphene, with the highest measured Young's modulus (~1
6   TPa) [3], is the most widely studied 2D material. Studies have shown that graphene filled into
7   the polymer matrices can reinforce the mechanical properties of the composites significantly
8   [8]. However, pristine graphene does not have a bandgap [9], which limits its applications in
9   certain fields requiring a semiconducting material. As a potential substitute material of graphene,
10   the transition metal dichalcogenides (TMDCs, e.g., MoS_2 and WSe_2) and black phosphorus (BP)
11   with an intrinsic bandgap [10, 11] possess the potential for electronics and optoelectronics
12   applications [12–15] and open a new field for 2D materials study. Moreover, the existence of
13   piezoelectricity and the more sensitive piezoresistive effect in TMDCs compared with gra-
14   phene under mechanical deformation make them more interesting for innovative applica-
15   tions including tactile strain sensors [16], nanogenerators [17], and advanced
16   nanoelectromechanical systems (NEMS).

17   In this review, first, we introduce the common approaches used for fabricating suspended 2D
18   material structures. Then, characterization methods for extracting the in-plane and out-of-
19   plane mechanical properties of 2D materials are presented. A summary of the experimental
20   results is given. In the last section, we introduce the electrical output change of 2D materials
21   induced by mechanical deformation—piezoresistive and piezoelectric effects. In addition, we
22   provide some example applications of 2D materials that make use of their extraordinary
23   mechanical as well as mechanoelectric transduction properties.

2. Fabrication of suspended 2D materials

25   Generally, to measure the mechanical properties of 2D materials experimentally, a suspended
26   structure needs to be fabricated. There are mainly two ways of fabricating a structure sus-
27   pended with 2D materials. One approach is to transfer the 2D materials directly onto the
28   prepatterned substrates [3, 7, 18–23]. The other approach is to transfer the 2D materials on the
29   substrate first and then remove the sacrificial layer beneath the transferred 2D materials [24–
30   31]. **Figure 1(a)** and (b) shows the two schematics of the first fabrication approach, while **Figure**
31   **1(c)** shows the second approach.
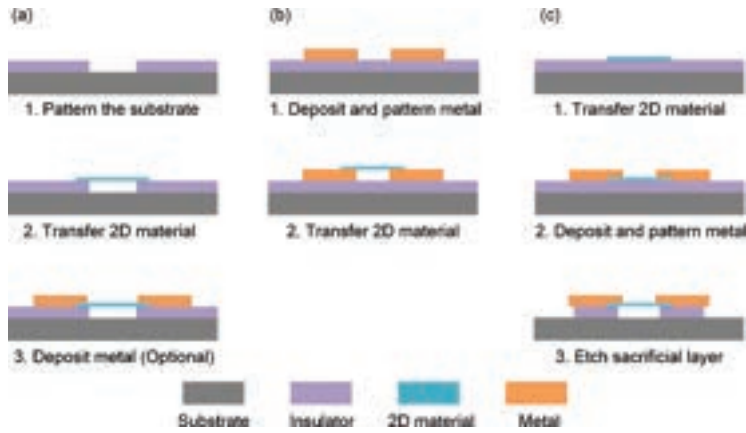
Figure 1. Schematic of two representative approaches of suspended structures fabrication. (a, b) Transfer of the 2D materials directly onto the prepatterned substrates; (c) Suspension of the 2D materials by etching the sacrificial layer underneath.

In the first approach, taking SiO_2/Si substrate for example, holes or cavities are patterned in the SiO_2 layer with lithography and wet/dry etching techniques, as shown in the first step of **Figure 1(a)**. Then, 2D materials are transferred onto the prepatterned SiO_2/Si substrate by the exfoliation method, forming suspended 2D materials structure (second step of **Figure 1(a)**). With this method, the suspended structure can be fabricated theoretically on various kinds of substrates. However, with the conventional mechanical exfoliation method, since the 2D material sheets distribute randomly onto the substrates, the 2D material sheets may not cover necessarily the specific hole in the SiO_2 layers, bringing the challenge of improving the production rate. Normally, two methods can be employed to address this problem. One method is to fabricate repeatable patterns (e.g., hole arrays) in the substrate [3, 7, 22] to enhance the probability of producing the suspended structures, as shown in **Figure 2(a)**. Another method is to employ a modified exfoliation method (transfer printing/stamping [20, 32]), with a transparent viscoelastic material as the carrier for the 2D materials, which enables a precise transfer of 2D materials to the desirable location [19, 21].

Figure 2. (a) Optical image of graphene suspended over hole arrays [35]. (b) SEM images of a MoS_2 bridge supported on Au electrodes [23]. (c) SEM image of suspended graphene stripe under Au electrodes [25].

1   In most cases, electrical signal needs to be applied to the suspended 2D materials; therefore,
2   metal contacts need to be made to contact the suspended 2D materials, as shown in the third
3   step of **Figure 1(a)**. In order to avoid the common wet process inducing the collapse of 2D
4   membranes, the shadow mask method [27] instead of lithography should be used. In addition,
5   by combining conventional lithography, lift-off of deposited metal and transfer printing/
6   stamping of 2D materials, one can realize the fabrication of suspended 2D materials supported
7   on patterned metal contacts, as depicted in **Figures 1(b)** and **2(b)**.

8   The schematic of the second approach of fabricating a suspended 2D material structure is
9   presented in **Figure 1(c)**. After the transfer of 2D material onto substrate and metal contacts
10 deposition, the 2D material is suspended by etching the underlying sacrificial layer with the
11 predeposited metal contacts acting as the etching mask and clamping of the 2D materials. In
12 this method, SiO_2 has been used widely as the sacrificial layer, which is removed commonly
13 by anisotropic wet etching with buffered hydrofluoric acid (BOE). In order to prevent the 2D
14 materials from collapsing due to the surface tension between the 2D materials and BOE, the
15 drying process is operated normally in a critical point dryer (CPD) [25, 29, 30]. In addition, the
16 etching time needs to be adjusted carefully to control the undercut of SiO_2 beneath the metal
17 contacts. Although a more complex structure can be fabricated with this approach, as shown
18 in **Figure 2(b)**, the wet etching involved in the fabrication process may introduce some
19 contamination in the 2D materials, which may degrade the performance of the devices.
20 Moreover, the acids used in this process are not suitable for some 2D materials, such as Bi_2Se_3
21 [33] and metals (e.g., Ti, Al). Thus, to avoid acid etching in the fabrication process, photoresist
22 can be used as the sacrificial layer instead of SiO_2 which can be removed with photoresist
23 developers [33, 34].   AQ2

24 ## 3. Mechanical properties

25 As mentioned earlier, 2D materials possess high anisotropy between the in-plane and out-of-
26 plane mechanical properties. In pristine-layered 2D materials, the nearby atoms in the same
27 plane are bonded covalently with low defects density resulting in strong in-plane mechanical
28 properties. While the interlayers are stacked together via weak van der Waals interactions,
29 allowing layers to slide easily when shear stress is applied, the effect can give rise to lubrication
30 properties. In this section, the experimental methods used to characterize the mechanical
31 properties of 2D materials are introduced, and the corresponding empirical results are
32 summarized.

33 ### 3.1. In-plane properties

34 The in-plane mechanical properties (including the in-plane Young's modulus, pretension, and
35 breaking strength/strain) of 2D materials have been studied extensively in bending experi-
36 ments on suspended 2D sheets. In the bending experiments, atomic force microscope (AFM)
37 is used widely to characterize the deformation of the suspended sheets under a certain amount
38 of force. The force applied during the experiments can be divided into two categories:

1 concentrated force and distributed force. In the following subsections, all the mechanical
2 properties mentioned indicate the in-plane properties, unless stated otherwise.

3 *3.1.1. Applying concentrated force*

4 The indentation experiment conducted under AFM is one of the most popular methods for
5 measuring the mechanical properties of 2D materials. In most cases, an AFM probe indents
6 toward the center of the circular suspended 2D materials, as shown in **Figure 3(a)**. During the
7 indentation, the displacement of piezoelectric scanner ΔZ (when the AFM probe starts to
8 contact with the membrane) and the deflection of AFM probe d are recorded. The indentation
9 depth at the center of a membrane can be determined by $\delta = \Delta Z - d$, and the force applied from
10 the AFM tip onto the membrane can be derived from $F = k \times d$, where k is the spring constant
11 of the AFM probe, which can be calibrated via a reference cantilever [36] or calculated using
12 the Sader method [37, 38]. Then, the force F versus deformation δ curves of a suspended 2D
13 material can be extracted, as shown in **Figure 3(b)**. When the radius of the AFM tip r_{tip} is far
14 smaller than that of the hole r and the bending stiffness of the measured 2D material is
15 negligible (monolayer or few-layer), the $F - \delta$ curves can be approximated using the Schwering-
16 type solution, as Eq. (1) [3, 39, 40]:

$$F = \left(\sigma_0^{2D}\pi\right)\delta + \left(E^{2D}\frac{q^3}{r^2}\right)\delta^3, \tag{1}$$

17
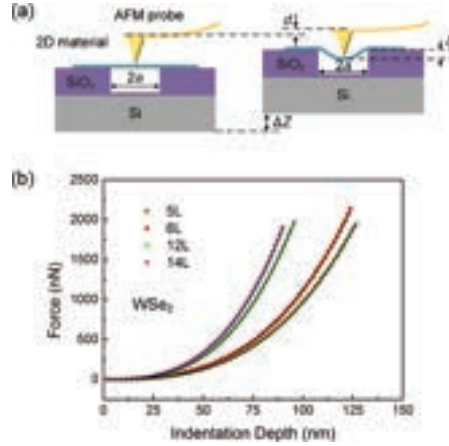
18 **Figure 3.** (a) Side view schematic of the indentation experiment on a suspended 2D membrane. (b) Representative
19 force–deformation curves for multilayer WSe$_2$. The fitted curves using the Schwering-type solution agree well with the
20 experimental results [42].

21 where σ_0^{2D} is the pretension, E^{2D} is the 2D elastic modulus, v is the Poisson's ratio, and q is a
22 dimensionless constant determined by $q = 1/(1.05 - 0.15v - 0.16v^2)$. By fitting the experimental

1   curves with Eq. (1), the pretension σ_0^{2D} and 2D elastic modulus E^{2D} of the membranes can be
2   derived. Due to the increasing thickness of 2D material (>15 nm) [41], the mechanical behavior
3   of 2D materials undergoes a membrane-to-plate regime transition, and therefore, the bending
4   stiffness should be taken into consideration by adding another term into Eq. (1), thus, forming
5   a modified model [6] which gives a better estimation of the pretension σ_0^{2D}:

$$F = \left[\frac{4\pi E^{2D}}{3(1-\upsilon^2)} \cdot \left(\frac{t}{r}\right)^2 \right]\delta + \left(\sigma_0^{2D}\pi\right)\delta + \left(E^{2D}\frac{q^3}{r^2}\right)\delta^3, \tag{2}$$

AQ3

6   where t is the thickness of the measured 2D material.

7   During an indentation experiment with a spherical indenter, the maximum stress for a circular
8   and linear elastic membrane as a function of the applied force F can be derived with the
9   expression as follows [43]:

$$\sigma_{max}^{2D} = \sqrt{\frac{FE^{2D}}{4\pi r_{tip}}}, \tag{3}$$

10   where σ_{max}^{2D} is the maximum stress at the center of the film (under the AFM tip). Thus, the
11   breaking stress of the 2D material can be estimated by acquiring the force which breaks the 2D
12   material during the indentation. Assuming the stress of the 2D material has a linear relation-
13   ship with its strain, the breaking strain can be predicted by $\varepsilon_{max} = \sigma_{max}^{2D}/E^{2D}$.

14   Apart from the circular membrane, the indentation experiment can be operated also at the
15   center of a beam-structured 2D material with two ends fixed [4, 44, 45]. In this case, the relation
16   between applied force F and deformation at the center of the 2D material δ can be modeled
17   with the expression [46]:

$$F = \frac{16E^{2D}wt^2}{l^3}\delta + \sigma_0^{2D}\delta + \frac{8wE^{2D}}{3l^3}\delta^3, \tag{4}$$

18   where l and w are the length and width of the suspended beam, respectively.

19   It is worth noting that it is extremely important to identify the zero displacement/force point
20   precisely for nanoindentation experiments [47]. An inaccuracy of 2–5 nm in determining this
21   point may lead to a 10% error in the extracted E^{2D} [35]. In order to compare the elastic properties
22   of a particular 2D material with its bulk counterpart as well as other 2D materials, the 2D elastic
23   modulus E^{2D} sometimes needs to be converted to the normal 3D Young's modulus E_y by
24   dividing the 2D value by the thickness of the 2D material t.

From the models of Eqs. (1), (2), and (4), we can see that the applied load has an approximate linear relationship with the indentation depth when the membrane deformation is small, and significantly follows a cubic relationship under large deformation. Thus, in the linear regime (small deformation of membrane), the effective spring constant of circular and beam-structured membrane can be extracted as

$$
k_{\text{circular}} = \frac{4\pi t^3}{3(1-\upsilon^2)r^2} E_{\text{Y}} + \sigma_0^{2D}\pi,
$$

$$
k_{\text{beam}} = \frac{16wt^3}{l^3} E_{\text{Y}} + \sigma_0^{2D}. \tag{5}
$$

By measuring the effective spring constant of the same kind of 2D material with different design, thickness t, or dimensions (r, w, or l), the Young's modulus E_{Y} and pretension σ_0^{2D} can be extracted. Note that this method is only valid under the assumption that E_{y} and σ_0^{2D} are independent on the thickness or dimension of the 2D material, assumptions of which are under debate at present [48, 49].

3.1.2. Applying distributed force

Apart from the concentrated force applied with an indenter, distributed force (such as electrostatic force [50] or pressure force [51]) can be applied on suspended 2D material to measure the mechanical properties. In order to produce an electrostatic force, metal contacts need to be made on/below 2D membrane, so that a voltage can be applied between the membrane and the back-gate electrode, as shown in **Figure 4(a)** and **(b)**. Moreover, by creating a pressure difference between the inside of microcavities covered by the 2D membrane p_{int} and the outside atmosphere p_{ext}, a pressure force Δp can be produced, as depicted in **Figure 4(c)** and **(d)**. The deformation of a membrane under distributed force can be characterized directly via tapping mode AFM (**Figure 4(e)**). In addition, by measuring the Raman shift of 2D material under loading and without loading, the local strain of 2D material can be extracted indirectly [49]. After building a specific mechanical model which describes the relationship of the deformation of the membrane due to the voltage bias [50] or pressure difference [51, 52], the mechanical properties can be extracted by fitting the experimental results with the appropriate model.
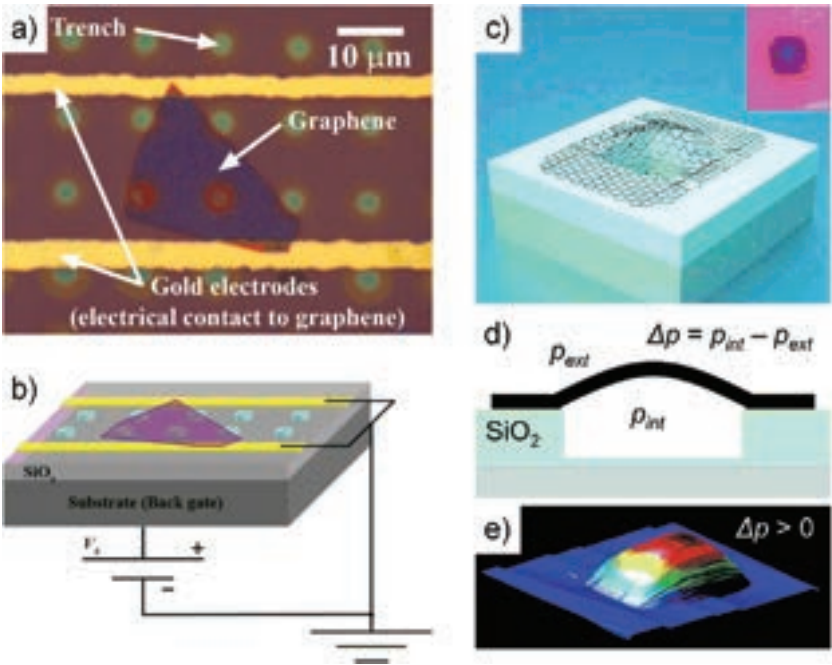
Figure 4. (a) Top view optical image of a graphene suspended over hole arrays. (b) Schematic of producing electrostatic force by applying a voltage V_S across the back gate and graphene [50]. (c) Schematic of a graphene-sealed microchamber. Inset: Optical image of a graphene membrane over a hole. (d) Side view schematic of the graphene-sealed microchamber. (e) Tapping mode AFM image of a graphene membrane with $\Delta p > 0$ [52].

3.1.3. Results summary

Table 1 summarizes the mechanical properties of 2D material families ranging from conductors (graphene), semiconductors (semiconducting TMDCs and BP), to dielectrics (graphene oxide [GO], mica, and h-BN). Overall, the Young's modulus of 2D materials is larger than that of the corresponding bulk materials, due to the lower crystal defects and interlayer stacking faults in 2D materials [6].

Material	Number of layers	Young's modulus (GPa)	Pretension (mN/m)	Breaking stress (GPa)	Breaking strain (%)	Characterization method	Ref.
Graphene (Mechanical exfoliated)	1	1000 ± 100	70–740	130 ± 10	~12	Indentation on circular membrane	[3]
	23–43	~1000	N/A	N/A	N/A	Electrostatic force	[50]
	4	930 ± 48	N/A	N/A	N/A	Pressurizing membranes	[52]

Material	Number of layers	Young's modulus (GPa)	Pretension (mN/m)	Breaking stress (GPa)	Breaking strain (%)	Characterization method	Ref.
	1–5	1000 ± 31	N/A	N/A	N/A	Pressurizing membranes	[51]
	1, 2	2400 ± 400 (1 L) 2000 ± 500 (2 L)	N/A	N/A	N/A	Pressurizing membranes	[49]
	3–14	~800	N/A	N/A	N/A	Indentation on beam	[46]
Graphene (Mechanical exfoliated + Ar plasma irradiation)	1	~1550	200–800	80–94	N/A	Indentation on circular membrane	[35]
Graphene (GO reduced)	1	250 ± 150	N/A	N/A	N/A	Spring constant of beam	[4]
Graphene (CVD growth)	1	~157	~85	~35	N/A	Indentation on circular membrane	[55]
	1	~1000	N/A	~121 (small grains) ~140 (large grains)	N/A	Indentation on circular membrane	[56]
	1	~800	~100	~55	N/A	Indentation on circular membrane	[47]
MoS_2 (Mechanical exfoliated)	1, 2	270 ± 100 (1 L) 200 ± 60 (2 L)	20–100	22 ± 4 (1 L) 21 ± 6 (2 L)	6–11	Indentation on circular membrane	[7]
	5–25	300 ± 10	0.15 ± 0.15	N/A	N/A	Spring constant of circular membrane	[59]
	5–25	330 ± 70	50 ± 20	N/A	N/A	Indentation on circular membrane	[6]
MoS_2 (CVD growth)	1, 2	260 ± 18 (1 L) 231 ± 10 (2 L)	110 ± 40 (1 L)	N/A	N/A	Indentation on circular membrane	[48]
WS_2 (CVD growth)	1	272 ± 18	150 ± 30	N/A	N/A	Indentation on circular membrane	[48]
WSe_2 (Mechanical exfoliated)	5, 6, 12, 14	170 ± 7 (5 L) 166 ± 6 (6 L) 168 ± 7 (12 L) 165 ± 6 (14 L)	638 ± 22 (5 L) 691 ± 37 (6 L) 499 ± 34 (12 L) 137 ± 26 (14 L)	>12	>7.3	Indentation on circular membrane	[42]
BP (Mechanical exfoliated)	17–35	27 ± 4 (armchair direction)	N/A	2.2 (armchair direction) 4.2 (zigzag direction)	7.2 (armchair direction)	Spring constant of beam	[54]

Material	Number of layers	Young's modulus (GPa)	Pretension (mN/m)	Breaking stress (GPa)	Breaking strain (%)	Characterization method	Ref.
		59 ± 12 (zigzag direction)			6.5 (zigzag direction)		
	17, 37	276 ± 32 (17 L) 90 ± 6.4 (37 L)	180–1200	>25	>8	Indentation on circular membrane	[41]
GO (Solution-based deposition)	1–3	208 ± 23 (1 L) 224 ± 18 (2 L) 230 ± 27 (3 L)	54 ± 14 (1 L) 32 ± 6 (2 L) 28 ± 4 (3 L)	N/A	N/A	Indentation on circular membrane	[57]
Mica (Mechanical exfoliated)	2–14	202 ± 22	140 ± 80	4–9	2–4.5	Indentation on circular membrane	[60]
h-BN (CVD growth)	2, 4, 5	279 ± 20 (2 L) 269 ± 13 (4 L) 252 ± 15 (5 L)	8.8 ± 1.2 (2 L) 12.8 ± 1.3 (4 L) 15.7 ± 1.5 (5 L)	~9	2.2	Indentation on circular membrane	[2]

Table 1. Summary of the in-plane mechanical properties of 2D materials measured from experiments.

3.1.3.1 Young's modulus

Pristine monolayer graphene (prepared by mechanical exfoliation from bulk graphite) is reported to be the stiffest 2D material on earth so far with a Young's modulus of approximately 1 TPa [3, 49, 51], because of the strong in-plane covalent carbon–carbon bonds. For 2D TMDCs—MX_2 (M = Mo, W; X = S, Se) with the same crystal structure (chalcogen atoms in two hexagonal planes separated by a plane of transition metal atoms) [11], a smaller Young's modulus of WSe_2 has been observed compared with MoS_2 and WS_2 [42]; due to a decrease in the charge transfer and an increase in the lattice constant, resulting in a weakened binding between the metal and chalcogen [53], as M changes from Mo to W and X changes from S to Se.

Meanwhile, the Young's modulus of some 2D materials (e.g., MoS_2, BP, and h-BN) [2, 7, 41, 48] have been found to decrease with an increase in their thickness (number of layers), which is caused mainly by interlayer stacking errors. The occurrence of interlayer sliding in multi-layer 2D materials during indentation is also a factor for underestimating the intrinsic Young's modulus [7]. However, the Young's modulus of WSe_2 remains unchanged statistically with increasing number of layers, which possibly results from the strong interlayer interaction in WSe_2 [42]. As stated earlier, for 2D materials with thickness-dependent Young's modulus, precaution needs to be taken when using model Eq. (5) to derive the Young's modulus. Furthermore, the highly anisotropic atomic structure in 2D materials, such as BP, presents an anisotropic Young's modulus along the different crystal orientations [54].

In addition, the mechanical properties of 2D materials largely depend on the density of crystal defects and thus are related to the preparation methods. For instance, the larger number of vacancy defects in the GO-reduced graphene and the existence of voids at the grain boundaries,

together with wrinkles in polycrystalline graphene prepared by the CVD method, can contribute to the weaker mechanical properties [4, 55]. In addition, the presence of a larger number of grain boundaries can affect the Young's modulus of 2D materials negatively [56]. By optimizing the processing steps of suspended 2D materials fabrication, the quantity of crystal defects and wrinkles in 2D materials can be reduced, thus leading to an improvement of the mechanical properties [56]. Research has shown that the elastic properties can be recovered by flattening the wrinkles in CVD graphene with a small prestretch [47]. The mechanical properties of 2D materials can be improved also by introducing controlled density of defects, such as Ar^+ plasma irradiation [35].

3.1.3.2. Pretension

The factors that can affect the pretension in 2D materials are quite complicated. The pretension not only depends on the intrinsic mechanical properties of 2D materials, but also on the fabrication process of the suspended structure (e.g., the method of transferring 2D material onto the substrates). Therefore, the pretension values of suspended 2D materials in **Table 1** vary greatly. Generally, the dry transfer process with scotch tape or viscoelastic stamp introduces higher pretension compared with wet transfer process such as solution-based deposition [57]. Suspended structures fabricated by etching sacrificial layer (method shown in **Figure 1(c)**) normally possess less pretension than 2D materials transferred directly onto prepatterned substrates (method shown in **Figure 1(a)** and **(b)**). Annealing, as a common method to remove the residue on 2D materials left over by a fabrication process, can introduce thermal stress due to the different thermal expansion coefficients between the substrates and the 2D materials.

3.1.3.3. Breaking strength

As presented in **Table 1**, the 2D materials with higher Young's modulus normally possess higher breaking strength. Many reports have found that the breaking stress of 2D materials can reach the theoretical upper limit ($E_Y/9$) [7], due to low disorder and impurities in the characterized 2D materials. The existence of anisotropic breaking strength along armchair and zigzag directions has been found in BP, possibly resulting from its anisotropic Young's modulus [54]. Except for the 2D dielectrics (mica and h-BN), the breaking strain of most 2D materials is above 7%, which is comparable with the common materials used as substrates for flexible electronics, namely polyimide (PI) or polydimethylsiloxane (PDMS) [58], implying that most of the 2D materials are compatible with flexible electronic devices.   AQ4

3.2. Out-of-plane properties

The research on the out-of-plane mechanical properties of 2D materials includes characterizing the elasticity perpendicular to the plane's direction and the interlayer shear force constant/strength parallel to the plane's direction. Unlike the experiments already conducted in characterizing the in-plane mechanical properties of 2D materials, experimental investigations on quantifying the out-of-plane properties are still quite scarce, mainly because of the technical difficulties in characterization [61]. Overall, out-of-plane properties can be explored directly

1   by applying normal/shear force to 2D materials or indirectly via Raman spectroscopy. This
2   section introduces the various experiments conducted thus far related to the measurements of
3   out-of-plane properties.

4   *3.2.1. Direct characterization*

5   *3.2.1.1. Perpendicular-to-plane elasticity*

6   Direct investigation of the perpendicular-to-plane elasticity of few-layer 2D materials remains
7   challenging, because extremely small indentations need to be conducted on supported 2D
8   sheets. Since the interlayer distance of 2D materials is so small (<1 nm), the maximum inden-
9   tation depth should be only a few angstroms (smaller than the interlayer distance) [62].

10   An unconventional AFM-based method (modulated nanoindentation, as shown in **Figure
11   5(a)**) with a high indentation depth resolution of 0.1 Å [63, 64] has been employed to measure
12   the perpendicular-to-plane elasticity of highly oriented pyrolytic graphite (HOPG), epitaxial
13   graphene (EG), epitaxial graphene oxide (EGO), and conventional GO successfully [62].
14   During the indentation, the AFM tip oscillates at 1 kHz frequency with an amplitude of
15   approximately 0.1 Å (ΔZ_{piezo}) controlled by a piezoelectric tube. The AFM feedback loop sets
16   a normal force F_z applied on the 2D materials from the AFM tip by setting the position of the
17   piezoelectric tube vertically. A tip oscillation with an amplitude of ΔZ_{piezo} results in a variation
18   of the normal force ΔF_z monitored via the deflection of a cantilever. At a certain normal force
19   F_z, the tip–2D material contact stiffness $k_{contact}$ can be obtained via the expression below:

$$\frac{\Delta F_Z}{\Delta Z_{piezo}} = \left(\frac{1}{k_{lever}} + \frac{1}{k_{contact}(F_Z)} \right)^{-1}, \tag{6}$$

20
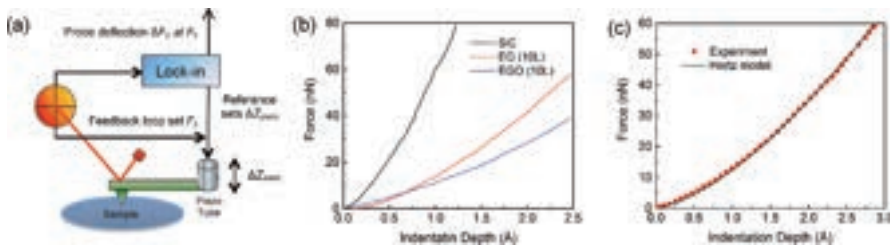
Figure 5. (a) Schematic of modulated nanoindentation on 2D materials. (b) Force–indentation curves for SiC, 10-layer
EG, and 10-layer EGO extracted from the nanoindentation. (c) Force–indentation curve for HOPG and the Hertzian
fitting. Adapted from Gao et al. [62].

24   where k_{lever} is the spring constant of the AFM cantilever. Then, the force F_z versus indentation
25   depth Z_{indent} curves (as shown in **Figure 5(b)**) can be derived by integrating $dF_z = k_{contact}(F_z)$
26   dZ_{indent} as

$$Z_{\text{indent}} = \int_0^{F_Z} \frac{dF_Z}{k_{\text{contact}}(F_Z)}. \tag{7}$$

When the indentation depth is in the subnanometer regime, the perpendicular Young's modulus can be extracted by fitting the $F_z - Z_{\text{indent}}$ curves with the Hertz model (as shown in **Figure 5(c)**):

$$F = \frac{4}{3} E^* r^{1/2} Z_{\text{indent}}^{2/3}, \tag{8}$$

where $E^* = \left(1 - (v^{\text{sample}})^2 / E_Y^{\text{sample}}\right) + \left(1 - (v^{\text{tip}})^2 / E_Y^{\text{tip}}\right)$, with v^{sample}, v^{tip}, E_Y^{sample}, and E_Y^{tip} being the Poisson's ratio and Young's modulus of the measured 2D material and AFM tip, respectively. With this approach, the perpendicular Young's modulus of HOPG, EG, EGO, and conventional GO is measured to be 33 ± 3 GPa, 36 ± 3 GPa, 23 ± 4 GPa, and 35 ± 10 GPa, respectively, which is far smaller than the in-plane Young's modulus. In addition, the intercalated water between GO layers can affect the perpendicular Young's modulus significantly. This method is very sensitive to the 2D material/substrate interaction and the number of layers of 2D material, and thus is useful for investigating 2D material/substrate interaction [62].

3.2.1.2. Shear force constant/strength

To measure the interlayer shear force constant/strength, proper shear stress should be applied to the interlayer interface of a 2D material using a probe. Oviedo et al. [61] have measured the interlayer shear strength of MoS$_2$ with a shearing strength test under in situ transmission electron microscopy (TEM) characterization, as shown in **Figure 6**. During the test, a multilayer MoS$_2$ flake sandwiched between a 3.5 μm thick focused ion beam (FIB)-deposited platinum (Pt) cap and a SiO$_2$/Si substrate has been attached to a piezoelectric manipulator, as shown in **Figure 6(a)**. Then, the sample has been moved toward a static indenter probe (attached to a force sensor) to apply force to the side of the Pt cap, thus creating shear stress in the MoS$_2$ flake (**Figure 6(b)**). During the test, the force versus distance plot has been recorded, as depicted in **Figure 6(c)**. With the force triggering the shear $F = 498.8 \pm 1.6$ μN and the sheared area $A = 19.7 \pm 0.5$ μm^2 (inset of **Figure 6(c)**), the shear strength of MoS$_2$ is calculated to be 25.3 ± 0.6 MPa, about 0.1% of in-plane Young's modulus (~260 GPa).

Another method to apply shear stress is to conduct friction force microscopy (FFM) measurements. In contrast to the approach mentioned earlier, the probe, applying normal force to the planes, is placed on the top surface of the 2D material sheets. Only when the probe–layer interactions are stronger than the interlayer interactions, shear stress can be applied in the 2D material by moving the probe laterally. The challenge of this approach is whether shear stress can be transferred from the probe to the interlayer interface of the measured samples efficiently. In addition, this method is not suitable to measure the shear strength with zero normal load. With this approach, shear strengths of graphite have been measured to be 0.27–0.75 MPa

depending on the sliding direction [65]. Meanwhile, the self-retracting motion of graphite, when the probe is removed away after loading, has been observed (shown in **Figure 7(a)** and **(b)**). Moreover, a set of lock-in states has been observed at certain rotation angles with 60° intervals, which requires an external force to unlock a lock-in state [66], as shown in **Figure 7(c)** and **(d)**. The interlayer shear strength of graphite where the lock-in appears is measured to be approximately 0.14 GPa [67].
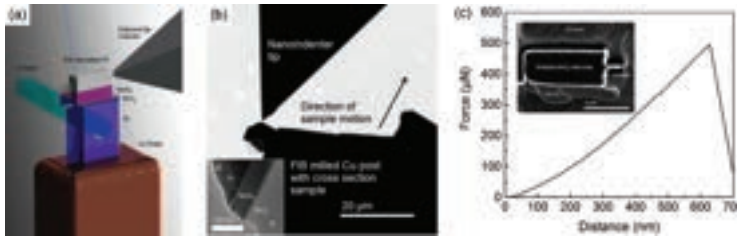
Figure 6. (a) Schematic of the in situ TEM shearing test. (b) Low-magnification TEM image of the indenter tip pointing to the test sample. Inset: High-magnification TEM image of the test sample. (c) Force versus distance plot recorded during the test. Inset: Top-view SEM image of the sheared surface. Adapted from Oviedo et al. [61].
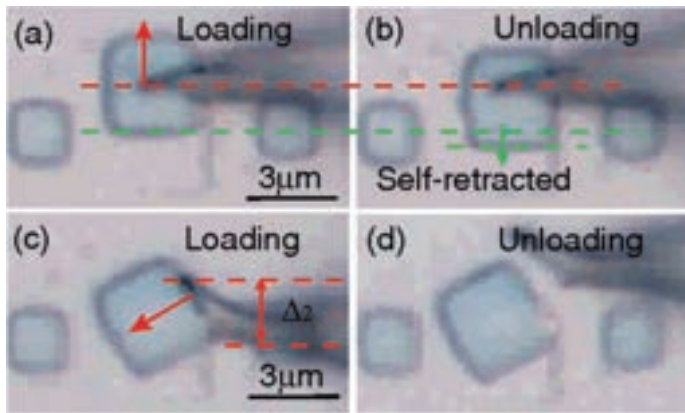
Figure 7. (a, b) Motion of a graphite flake that self-retracts after unloading. (c, d) Motion of a graphite that is in a lock-in state [66].

3.2.2. Raman spectroscopy

Furthermore, the interlayer interaction of 2D materials can be investigated using Raman spectroscopy. By probing the interlayer phonons modes, both the parallel-to-plane (shear) and perpendicular-to-plane (breathing) interlayer force constants can be extracted from the Raman spectrum. Since interlayer vibrational modes are usually in the low-frequency regime, due to the weak interlayer van der Waals restoring force, a special filter in Raman spectroscopy needs

to be used to suppress the Rayleigh scattering background [68, 69]. Alternatively, the interlayer interaction can be investigated from the Raman spectrum of folded 2D sheets with enhanced interlayer vibrational modes response [70]. The interlayer breathing mode or shear mode force constants can be obtained by fitting the experimental frequency of the ith vibrational mode, with the expression below [68]:

$$\omega_i = \sqrt{\frac{k}{2\mu\pi^2 c^2}\left(1 - \cos\left(\frac{(i-1)\pi}{N}\right)\right)}, \tag{9}$$

where k is the breathing/shear mode force constant per unit area; c is the speed of light; μ and N are the mass per unit area and the number of layers of the 2D material, respectively. **Table 2** summarizes the shear and breathing mode force constants measured with this method. Generally, breathing mode force constant is about two to three times larger than that of shear mode, which is possibly the reason why shear exfoliation can enhance the exfoliation efficiency significantly compared with conventional exfoliation methods [71]. The interlayer interaction of multilayer graphene is reported to be the weakest so far. On the other hand, the large difference in the shear elastic modulus along two different in-plane directions reflects the strong anisotropic elastic properties of BP [72].   AQ5

| Materials	Number of layers	Force constants ($\times 10^{19}$ N/m^3)		Ref.
		Shear mode	Breathing mode	
Graphene	2–5	1.28	NA	[68]
MoS$_2$	2–9	2.72	8.62	[69]
WSe$_2$	2, 4	3.07	8.63	
BP	4–14	1.70 (armchair direction)	12.3	[72]
		3.82 (zigzag direction)		
Bi$_2$Te$_3$	2–8	4.57	13.33	[73]
Bi$_2$Se$_3$	2–6	2.27	5.26	

Table 2. Interlayer shear/breathing mode force constants extracted from Raman spectroscopy.

4. Applications

4.1. Flexible transistor

The combination of high breaking strain, low thickness, and versatile electronic properties of 2D materials make them competitive contenders for flexible electronics applications. Because of the semiconducting properties, certain TMDCs (such as MoS$_2$, WS$_2$, and WSe$_2$) and BP can be used as channel materials in flexible transistors, while pristine graphene with relative high

conductivity is suitable as an electrode material. Mica and h-BN with large bandgaps can be used for 2D gate dielectrics [74, 75]. **Figure 8(a)** shows a flexible and transparent thin film transistor (TFT) fabricated from all 2D materials on a polyethylene terephthalate (PET)-flexible substrate [76]. The structure of the TFT is depicted in the inset of **Figure 8(b)**. As shown in **Figure 8(b)**, the current On/Off ratio has been found to be about 7.5×10^3, exhibiting p-type FET characteristics, and the device characteristics have been unaltered within a mechanical strain of 2%. **Figure 8(c)** shows the output characteristics of the flexible TFT with the characteristic of current saturation similar to conventional Si transistors, uncovering the great potential application of 2D materials in flexible transistors.
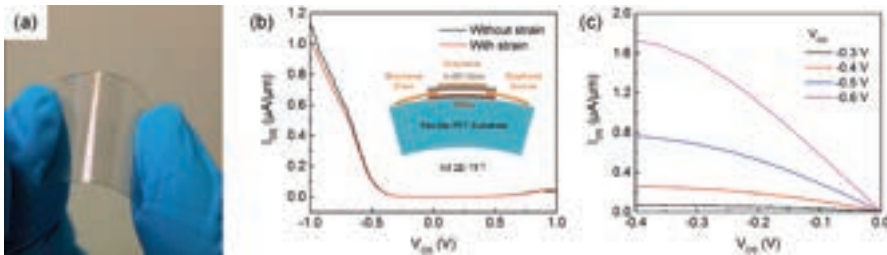

Figure 8. (a) All 2D materials-based TFTs on a flexible PET substrate. (b) Transfer characteristics of the TFT with and without 2% strain. Inset: Side-view schematic of the flexible TFT. (c) Output characteristics of the TFT. Adapted from Das et al. [76].
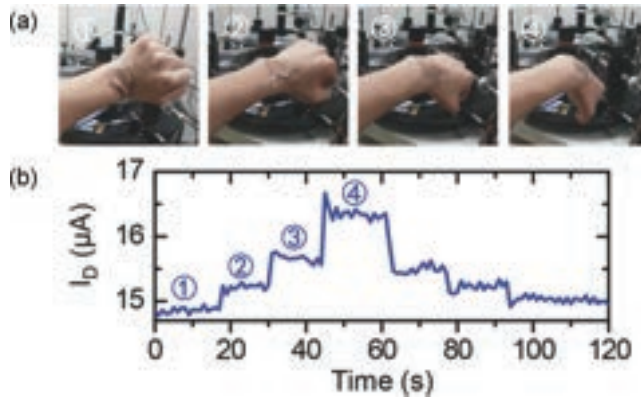
4.2. Strain sensor

The 2D materials [77, 78] have been found to undergo band structure change under applied strain. In addition, the distortion of the 2D films may result in additional scattering, thus reducing the carrier mobility [79]. The above factors contribute to a piezoresistive effect, in which the resistivity of 2D materials is modulated by mechanical deformation. Thus, 2D materials can be used as strain or pressure sensor [80, 81], by taking advantage of the piezoresistive effects. The sensitivity of a strain sensor is characterized usually by its gauge factor (GF), defined as $\left[\Delta R(\varepsilon)/R_0\right]/\varepsilon$, where R_0 is the total resistance of the unstrained device and $\Delta R(\varepsilon)$ is the resistance change under strain ε. The GF of pristine graphene has been characterized to be about 2 [81–85] due to the zero bandgap and the large strain required to open the bandgap, which can be a disadvantage for strain sensors. On the other hand, the GF of MoS_2 can reach approximately −200 [17, 29], resulting from the higher sensitivity of the decreasing bandgap and the direct–indirect bandgap transition under tensile strain, making MoS_2 more suitable for strain-sensing systems. The sensing performance of the 2D strain sensor can be enhanced by optimizing the structure design, such as the piezopotential-gated graphene matrix sensor arrays (GF = 389, as shown in **Figure 9(a)**) [16], quasi-continuous nanographene film sensor (GF = 507, as shown in **Figure 9(b)**) [86, 87], and graphene-woven fabric sensor (GF = 1000) [88, 89].
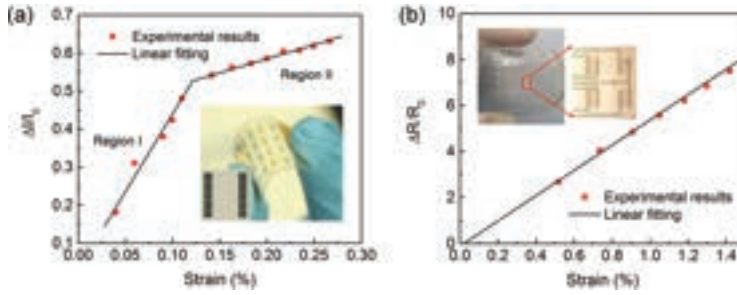
Figure 9. Sensing characteristics of the (a) piezopotential-gated graphene matrix strain sensor (Adapted from Sun et al. [16]) and (b) quasi-continuous nanographene film strain sensor (Adapted from Zhao et al. [86]).

Moreover, the piezoresistive effect, combined with the high breaking strain of 2D materials enable the design of wearable strain sensors for human motion detection. **Figure 10(a)** shows a prototype of tactile sensor fabricated with graphene films on a PDMS substrate attached on the human wrist. As shown in **Figure 10(b)**, the test subject's motions can be captured clearly with the strain sensor by outputting varying current response under different motions [16].


Figure 10. (a) A graphene tactile strain sensor attached on the wrist detecting the hand motion. (b) The electrical response of the tactile strain sensor in different hand motions shown in (a) [16].

4.3. Nanogenerator

Research has shown that odd-layer TMDCs possess piezoelectric property due to the absence of inversion symmetry [17, 34]. **Figure 11(a)** shows a flexible device with the monolayer MoS_2 flake outlined with black dashed line. When the substrate is bent from the two ends mechanically, the MoS_2 flake will be stretched, and piezoelectric polarization charges will be induced at the zigzag edges of the MoS_2 flake which can drive the flow of electrons in an external circuit as depicted in **Figure 11(e)**. When the substrate is released, electrons flow back

1   in the opposite direction as shown in **Figure 11(f)**. **Figure 11(b)** and **(c)** show that periodic
2   stretching and releasing of the substrate can generate piezoelectric outputs in the external
3   circuit with alternating polarity, which converts mechanical energy into electricity. A maxi-
4   mum mechanical-to-electrical energy conversion efficiency of 5.08% can be achieved from the
5   device [17]. The existence of piezoelectricity, coupled with the mechanical flexibility of some
6   2D materials, demonstrates their potential applications in wearable power-generated nano-
7   devices.

8
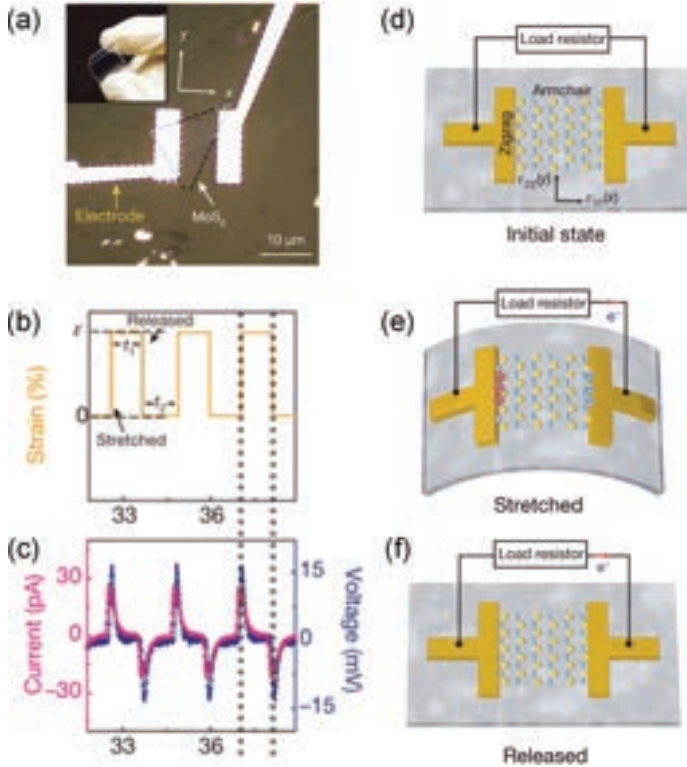
9   **Figure 11.** (a) A flexible device with a monolayer MoS$_2$ flake and metal electrodes at its zigzag edges. (b) Applied peri-
10   odic strain as a function of time. (c) Corresponding piezoelectric outputs when strain is applied along the armchair
11   direction. Operation of the MoS$_2$-based piezoelectric device in initial state (d), stretched state (e), and released state (f)
12   [17].

13   **4.4. Resonator**

14   Nanoelectromechanical systems (NEMS) resonator, offering the potential for extreme mass
15   and force sensitivity [25, 90], has triggered intense interest in recent years. The resonant
16   frequency of the resonators depends greatly on their geometry and the mechanical properties
17   of the vibrational materials (such as Young's modulus and mass density) [91]. As the sensitivity

1   of resonators improves with increase in resonant frequency, 2D materials are prospective

2   materials for highly sensitive NEMS due to their extraordinary mechanical properties and low

3   mass. Among the family of 2D materials, graphene resonator has been studied most so far.

4   **Figure 12(a)** shows a schematic and a SEM image of a graphene resonator. **Figure 12(b)** shows

5   a schematic of the electrical actuation and detection of mechanical vibrations of the graphene

6   resonator. A dc voltage V_g applied to the gate causes static deflection of the graphene toward

7   the gate. The resonant motion is actuated by ac voltage with an amplitude of V_a and frequency

8   of ω_a applied to the drain electrode, and read out by the current mixing method [25] using a

9   lock-in amplifier. As shown in **Figure 12(c)**, when $V_g = 0$ V and $V_a = 250$ mV, the fundamental

10   resonance frequency (Peak A) is approximately 1 MHz, and the second vibration mode (Peak

11   B) is measured to be approximately 2 MHz. The amplitude of vibrational modes increases with

12   increasing V_a. However, the resonant frequency decreases as V_a increases due to nonlinear

13   damping effects at higher resonance amplitudes [92]. By operating the graphene resonant

14   sensors in the second mode regime, the detection sensitivity can be improved significantly [93].

15
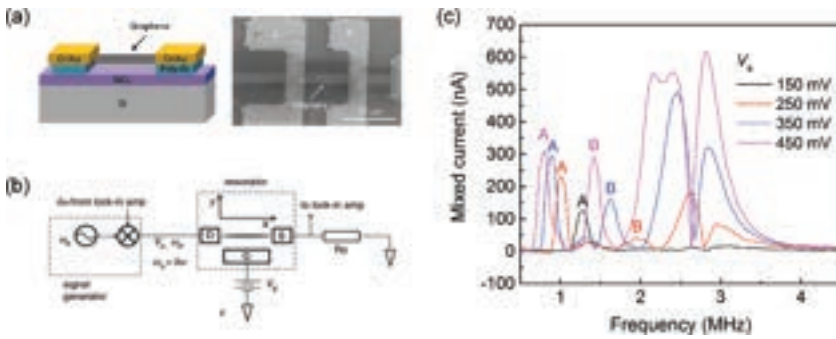
16   **Figure 12.** (a) Schematic and SEM image of a graphene resonator. (b) Circuit diagram of current-mixing characteriza-
17   tion setup. (c) The mixed current versus driving frequency for different amplitudes of actuation voltages. Adapted
18   from Chen et al. [93].

19   NEMS with low resonant frequency can be used for acoustic electronics, such as acoustic sensor

20   [94] and loudspeakers [95]. Since the resonant frequencies of resonators can be tuned inversely

21   by increasing the dimensions of vibrational parts, resonators with lower resonant frequencies

22   can be fabricated on 2D membranes with larger dimensions. **Figure 13** shows the response of

23   a graphene resonator working in the low-frequency regime [94]. The resonator has been

24   actuated with a piezoelectric disk driven with a sinusoidal signal and detected using a Laser

25   Doppler Vibrometer (LDV). The fundamental resonant frequency has been measured to be

26   approximately 16 kHz for a 3×3 mm^2 graphene membrane.
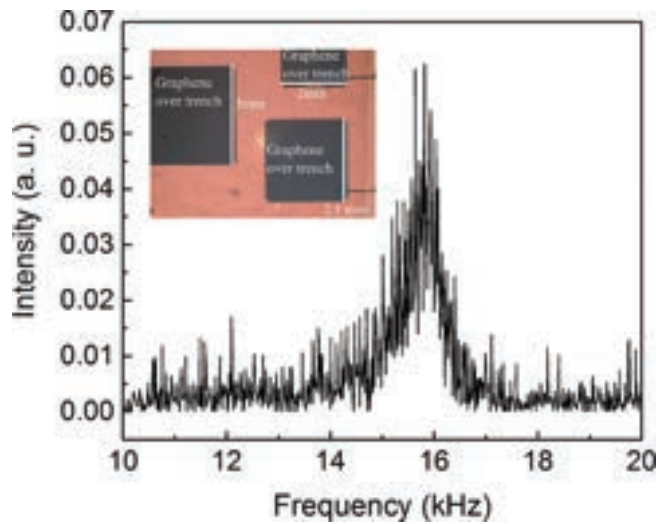
5. Conclusions

In this article, we have reviewed the experimental study of in-plane and out-of-plane mechanical properties of 2D materials ranging from conductors (e.g., graphene), semiconductors (e.g., TMDCs and BP), to insulators (e.g., h-BN). First, various approaches for fabricating suspended 2D material devices have been demonstrated, whose advantages and disadvantages have been compared. Then, the various characterization methods and the corresponding results have been summarized, with special focus being paid to the mechanical differences among the different 2D materials. With the extraordinary mechanical properties (ultralow weight, high Young's modulus, and high strength), 2D materials possess the potential for applications in flexible electronics and highly sensitive resonating mass sensors. The associated piezoresistive and piezoelectric effects under mechanical strain in 2D materials extend their applications to strain sensors, nanogenerators, and advanced NEMS.

Acknowledgements

Author details

Rui Zhang and Rebecca Cheung*

*Address all correspondence to: r.cheung@ed.ac.uk

Scottish Microelectronics Centre, The University of Edinburgh, Edinburgh, United Kingdom

References

[1] Novoselov KS, Geim AK, Morozov SV, Jiang D, Zhang Y, Dubonos SV, et al. Electric field effect in atomically thin carbon films. Science. 2004;306:666–669. DOI: 10.1126/science.1102896

[2] Song L, Ci L, Lu H, Sorokin PB, Jin C, Ni J, et al. Large scale growth and characterization of atomic hexagonal boron nitride layers. Nano Letters. 2010;10:3209–3215. DOI: 10.1021/nl1022139

[3] Lee C, Wei X, Kysar JW, Hone J. Measurement of the elastic properties and intrinsic strength of monolayer graphene. Science. 2008;321:385–388. DOI: 10.1126/science.1157996

[4] Gomez-Navarro C, Burghard M, Kern K. Elastic properties of chemically derived single graphene sheets. Nano Letters. 2008;8:2045–2049. DOI: 10.1021/nl801384y

[5] Song XF, Oksanen M, Sillanpaa MA, Craighead HG, Parpia JM, Hakonen PJ. Stamp transferred suspended graphene mechanical resonators for radio frequency electrical readout. Nano Letters. 2012;12:198–202. DOI: 10.1021/nl203305q

[6] Castellanos-Gomez A, Poot M, Steele GA, van der Zant HSJ, Agrait N, Rubio-Bollinger G. Elastic properties of freely suspended MoS_2 nanosheets. Advanced Materials. 2012;24:772–775. DOI: 10.1002/adma.201103965

[7] Bertolazzi S, Brivio J, Kis A. Stretching and breaking of ultrathin MoS_2. ACS Nano. 2011;5:9703–9709. DOI: 10.1021/nn203879f

[8] Zhao X, Zhang Q, Chen D, Lu P. Enhanced mechanical properties of graphene-based poly(vinyl alcohol) composites. Macromolecules. 2010;43:2357–2363. DOI: 10.1021/ma902862u

[9] Zhang Y, Tan Y-W, Stormer HL, Kim P. Experimental observation of the quantum Hall effect and Berry's phase in graphene. Nature. 2005;438:201–204. DOI: 10.1038/nature04235

[10]   Zhao W, Ghorannevis Z, Chu L, Toh M, Kloc C, Tan P-H, et al. Evolution of electronic structure in atomically thin sheets of WS_2 and WSe_2. ACS Nano. 2013;7:791–797. DOI: 10.1021/nn305275h

[11]   Wang QH, Kalantar-Zadeh K, Kis A, Coleman JN, Strano MS. Electronics and optoelectronics of two-dimensional transition metal dichalcogenides. Nature Nanotechnology. 2012;7:699–712. DOI: 10.1038/nnano.2012.193

[12]   Yoon J, Park W, Bae G-Y, Kim Y, Jang HS, Hyun Y, et al. Highly flexible and transparent multilayer mos_2 transistors with graphene electrodes. Small. 2013;9:3295–3300. DOI: 10.1002/smll.201300134

[13]   Wang H, Yu LL, Lee YH, Shi YM, Hsu A, Chin ML, et al. Integrated circuits based on bilayer MOS2 transistors. Nano Letters. 2012;12:4674–4680. DOI: 10.1021/nl302015v

[14]   Bertolazzi S, Krasnozhon D, Kis A. Nonvolatile memory cells based on mos_2/graphene heterostructures. ACS Nano. 2013;7:3246–3252. DOI: 10.1021/nn3059136

[15]   Lopez-Sanchez O, Lembke D, Kayci M, Radenovic A, Kis A. Ultrasensitive photodetectors based on monolayer MoS_2. Nature Nanotechnology. 2013;8:497–501. DOI: 10.1038/nnano.2013.100

[16]   Sun Q, Seung W, Kim BJ, Seo S, Kim S-W, Cho JH. Active matrix electronic skin strain sensor based on piezopotential-powered graphene transistors. Advanced Materials. 2015;27:3411–3417. DOI: 10.1002/adma.201500582

[17]   Wu W, Wang L, Li Y, Zhang F, Lin L, Niu S, et al. Piezoelectricity of single-atomic-layer MoS_2 for energy conversion and piezotronics. Nature. 2014;514:470–474. DOI: 10.1038/nature13792

[18]   Bunch JS, van der Zande AM, Verbridge SS, Frank IW, Tanenbaum DM, Parpia JM, et al. Electromechanical resonators from graphene sheets. Science. 2007;315:490–493. DOI: 10.1126/science.1136836

[19]   Choi K, Lee YT, Min S-W, Lee HS, Nam T, Kim H, et al. Direct imprinting of MoS_2 flakes on a patterned gate for nanosheet transistors. Journal of Materials Chemistry C. 2013;1:7803–7807. DOI: 10.1039/c3tc31796j

[20]   Castellanos-Gomez A, Buscema M, Molenaar R, Singh V, Janssen L, van der Zant HSJ, et al. Deterministic transfer of two-dimensional materials by all-dry viscoelastic stamping. 2D Materials. 2014;1:011002. DOI: 10.1088/2053-1583/1/1/011002

[21]   Yang R, Zheng X, Wang Z, Miller CJ, Feng PXL. Multilayer MoS_2 transistors enabled by a facile dry-transfer technique and thermal annealing. Journal of Vacuum Science & Technology B. 2014;32:061203. DOI: 10.1116/1.4898117

[22]   Li B, He Y, Lei S, Najmaei S, Gong Y, Wang X, et al. Scalable transfer of suspended two-dimensional single crystals. Nano Letters. 2015;15:5089–5097. DOI: 10.1021/acs.nanolett.5b01210

[23] Qiu D, Lee DU, Park CS, Lee KS, Kim EK. Transport properties of unrestricted carriers in bridge-channel MoS_2 field-effect transistors. Nanoscale. 2015;7:17556–17562. DOI: 10.1039/c5nr04397b

[24] van der Zande AM, Barton RA, Alden JS, Ruiz-Vargas CS, Whitney WS, Pham PHQ, et al. Large-scale arrays of single-layer graphene resonators. Nano Letters. 2010;10:4869–4873. DOI: 10.1021/nl102713c

[25] Chen CY, Rosenblatt S, Bolotin KI, Kalb W, Kim P, Kymissis I, et al. Performance of monolayer graphene nanomechanical resonators with electrical readout. Nature Nanotechnology. 2009;4:861–867. DOI: 10.1038/nnano.2009.267

[26] Bolotin KI, Sikes KJ, Jiang Z, Klima M, Fudenberg G, Hone J, et al. Ultrahigh electron mobility in suspended graphene. Solid State Communications. 2008;146:351–355. DOI: 10.1016/j.ssc.2008.02.024

[27] Bao W, Liu G, Zhao Z, Zhang H, Yan D, Deshpande A, et al. Lithography-free fabrication of high quality substrate-supported and freestanding graphene devices. Nano Research. 2010;3:98–102. DOI: 10.1007/s12274-010-1013-5

[28] Wang F, Stepanov P, Gray M, Lau CN. Annealing and transport studies of suspended molybdenum disulfide devices. Nanotechnology. 2015;26:105709. DOI: 10.1088/0957-4484/26/10/105709

[29] Manzeli S, Allain A, Ghadimi A, Kis A. Piezoresistivity and strain-induced band gap tuning in atomically thin MoS_2. Nano Letters. 2015;15:5330–5335. DOI: 10.1021/acs.nanolett.5b01689

[30] Jin T, Kang J, Su Kim E, Lee S, Lee C. Suspended single-layer MoS_2 devices. Journal of Applied Physics. 2013;114:164509. DOI: 10.1063/1.4827477

[31] Wang F, Stepanov P, Gray M, Lau CN, Itkis ME, Haddon RC. Ionic liquid gating of suspended mos_2 field effect transistor devices. Nano Letters. 2015;15:5284–5288. DOI: 10.1021/acs.nanolett.5b01610

[32] Meitl MA, Zhu ZT, Kumar V, Lee KJ, Feng X, Huang YY, et al. Transfer printing by kinetic control of adhesion to an elastomeric stamp. Nature Materials. 2006;5:33–38. DOI: 10.1038/nmat1532

[33] Velasco J, Jr., Zhao Z, Zhang H, Wang F, Wang Z, Kratz P, et al. Suspension and measurement of graphene and Bi_2Se_3 thin crystals. Nanotechnology. 2011;22:285305. DOI: 10.1088/0957-4484/22/28/285305

[34] Zhu H, Wang Y, Xiao J, Liu M, Xiong S, Wong ZJ, et al. Observation of piezoelectricity in free-standing monolayer MoS_2. Nature Nanotechnology. 2015;10:151–155. DOI: 10.1038/nnano.2014.309

[35] Lopez-Polin G, Gomez-Navarro C, Parente V, Guinea F, Katsnelson MI, Perez-Murano F, et al. Increasing the elastic modulus of graphene by controlled defect creation. Nature Physics. 2015;11:26–31. DOI: 10.1038/nphys3183

[36] Gates RS, Reitsma MG. Precise atomic force microscope cantilever spring constant calibration using a reference cantilever array. Review of Scientific Instruments. 2007;78:086101. DOI: 10.1063/1.2764372

[37] Sader JE, Chon JWM, Mulvaney P. Calibration of rectangular atomic force microscope cantilevers. Review of Scientific Instruments. 1999;70:3967–3969. DOI: 10.1063/1.1150021

[38] Sader JE, Sanelli JA, Adamson BD, Monty JP, Wei X, Crawford SA, et al. Spring constant calibration of atomic force microscope cantilevers of arbitrary shape. Review of Scientific Instruments. 2012;83:103705. DOI: 10.1063/1.4757398

[39] Komaragiri U, Begley MR, Simmonds JG. The mechanical response of freestanding circular elastic films under point and pressure loads. Journal of Applied Mechanics. 2005;72:203–212. DOI: 10.1115/1.1827246

[40] Begley MR, Mackin TJ. Spherical indentation of freestanding circular thin films in the membrane regime. Journal of the Mechanics and Physics of Solids. 2004;52:2005–2023. DOI: 10.1016/j.jmps.2004.03.002

[41] Wang J-Y, Li Y, Zhan Z-Y, Li T, Zhen L, Xu C-Y. Elastic properties of suspended black phosphorus nanosheets. Applied Physics Letters. 2016;108:013104. DOI: 10.1063/1.4939233

[42] Zhang R, Koutsos V, Cheung R. Elastic properties of suspended multilayer WSe_2. Applied Physics Letters. 2016;108:042104. DOI: 10.1063/1.4940982

[43] Bhatia NM, Nachbar W. Finite indentation of an elastic membrane by a spherical indenter. International Journal of Non-Linear Mechanics. 1968;3:307–324. DOI: 10.1016/0020-7462(68)90004-8

[44] Lindahl N, Midtvedt D, Svensson J, Nerushev OA, Lindvall N, Isacsson A, et al. Determination of the bending rigidity of graphene via electrostatic actuation of buckled membranes. Nano Letters. 2012;12:3526–3531. DOI: 10.1021/nl301080v

[45] Frank IW, Tanenbaum DM, van der Zande AM, McEuen PL. Mechanical properties of suspended graphene sheets. Journal of Vacuum Science & Technology B. 2007;25:2558–2561. DOI: 10.1116/1.2789446

[46] Li P, You Z, Haugstad G, Cui T. Graphene fixed-end beam arrays based on mechanical exfoliation. Applied Physics Letters. 2011;98:253105. DOI: 10.1063/1.3594242

[47] Lin Q-Y, Jing G, Zhou Y-B, Wang Y-F, Meng J, Bie Y-Q, et al. Stretch-induced stiffness enhancement of graphene grown by chemical vapor deposition. ACS Nano. 2013;7:1171–1177. DOI: 10.1021/nn3053999

[48] Liu K, Yan QM, Chen M, Fan W, Sun YH, Suh J, et al. Elastic properties of chemical-vapor-deposited monolayer mos_2, ws_2, and their bilayer heterostructures. Nano Letters. 2014;14:5097–5103. DOI: 10.1021/nl501793a

[49] Lee J-U, Yoon D, Cheong H. Estimation of young's modulus of graphene by raman spectroscopy. Nano Letters. 2012;12:4444–4448. DOI: 10.1021/nl301073q

[50] Wong CL, Annamalai M, Wang ZQ, Palaniapan M. Characterization of nanomechanical graphene drum structures. Journal of Micromechanics and Microengineering. 2010;20:115029. DOI: 10.1088/0960-1317/20/11/115029

[51] Koenig SP, Boddeti NG, Dunn ML, Bunch JS. Ultrastrong adhesion of graphene membranes. Nature Nanotechnology. 2011;6:543–546. DOI: 10.1038/nnano.2011.123

[52] Bunch JS, Verbridge SS, Alden JS, van der Zande AM, Parpia JM, Craighead HG, et al. Impermeable atomic membranes from graphene sheets. Nano Letters. 2008;8:2458–2462. DOI: 10.1021/nl801457b

[53] Zeng F, Zhang W-B, Tang B-Y. Electronic structures and elastic properties of monolayer and bilayer transition metal dichalcogenides MX2 (M= Mo, W;X= O, S, Se, Te): a comparative first-principles study. Chinese Physics B. 2015;24:097103. DOI: 10.1088/1674-1056/24/9/097103

[54] Tao J, Shen W, Wu S, Liu L, Feng Z, Wang C, et al. Mechanical and electrical anisotropy of few-layer black phosphorus. ACS Nano. 2015;9:11362–11370. DOI: 10.1021/acsnano.5b05151

[55] Ruiz-Vargas CS, Zhuang HL, Huang PY, van der Zande AM, Garg S, McEuen PL, et al. Softened elastic response and unzipping in chemical vapor deposition graphene membranes. Nano Letters. 2011;11:2259–2263. DOI: 10.1021/nl200429f

[56] Lee G-H, Cooper RC, An SJ, Lee S, van der Zande A, Petrone N, et al. High-strength chemical-vapor–deposited graphene and grain boundaries. Science. 2013;340:1073–1076. DOI: 10.1126/science.1235126

[57] Suk JW, Piner RD, An J, Ruoff RS. Mechanical properties of monolayer graphene oxide. ACS Nano. 2010;4:6557–6564. DOI: 10.1021/nn101781v

[58] Kim D-H, Ahn J-H, Choi WM, Kim H-S, Kim T-H, Song J, et al. Stretchable and foldable silicon integrated circuits. Science. 2008;320:507–511. DOI: 10.1126/science.1154367

[59] Castellanos-Gomez A, Poot M, Steele GA, van der Zant HSJ, Agrait N, Rubio-Bollinger G. Mechanical properties of freely suspended semiconducting graphene-like layers based on MoS2. Nanoscale Research Letters. 2012;7:1–4. DOI: 10.1186/1556-276x-7-233

[60] Castellanos-Gomez A, Poot M, Amor-Amoros A, Steele GA, van der Zant HSJ, Agrait N, et al. Mechanical properties of freely suspended atomically thin dielectric layers of mica. Nano Research. 2012;5:550–557. DOI: 10.1007/s12274-012-0240-3

[61] Oviedo JP, Kc S, Lu N, Wang J, Cho K, Wallace RM, et al. In situ TEM characterization of shear-stress-induced interlayer sliding in the cross section view of molybdenum disulfide. ACS Nano. 2015;9:1543–1551. DOI: 10.1021/nn506052d

[62] Gao Y, Kim S, Zhou S, Chiu H-C, Nelias D, Berger C, et al. Elastic coupling between layers in two-dimensional materials. Nature Materials. 2015;14:714–720. DOI: 10.1038/nmat4322

[63] Lucas M, Mai W, Yang R, Wang ZL, Riedo E. Aspect ratio dependence of the elastic properties of ZnO nanobelts. Nano Letters. 2007;7:1314–1317. DOI: 10.1021/nl070310g

[64] Palaci I, Fedrigo S, Brune H, Klinke C, Chen M, Riedo E. Radial elasticity of multiwalled carbon nanotubes. Physical Review Letters. 2005;94:175502. DOI: 10.1103/PhysRevLett.94.175502

[65] Zheng Q, Jiang B, Liu S, Weng Y, Lu L, Xue Q, et al. Self-retracting motion of graphite microflakes. Physical Review Letters. 2008;100:067205. DOI: 10.1103/PhysRevLett.100.067205

[66] Liu Z, Yang J, Grey F, Liu JZ, Liu Y, Wang Y, et al. Observation of microscale superlubricity in graphite. Physical Review Letters. 2012;108:205503. DOI: 10.1103/PhysRevLett.108.205503

[67] Liu Z, Zhang S-M, Yang J-R, Liu JZ, Yang Y-L, Zheng Q-S. Interlayer shear strength of single crystalline graphite. Acta Mechanica Sinica. 2012;28:978–982. DOI: 10.1007/s10409-012-0137-0

[68] Tan PH, Han WP, Zhao WJ, Wu ZH, Chang K, Wang H, et al. The shear mode of multilayer graphene. Nature Materials. 2012;11:294–300. DOI: 10.1038/nmat3245

[69] Zhao Y, Luo X, Li H, Zhang J, Araujo PT, Gan CK, et al. Inter layer breathing and shear modes in few-trilayer MoS_2 and WSe_2. Nano Letters. 2013;13:1007–1015. DOI: 10.1021/nl304169w

[70] Cong C, Yu T. Enhanced ultra-low-frequency interlayer shear modes in folded graphene layers. Nature Communications. 2014;5:4709. DOI: 10.1038/ncomms5709

[71] Chen M, Nam H, Rokni H, Wi S, Yoon JS, Chen P, et al. Nanoimprint-assisted shear exfoliation (NASE) for Producing multilayer MoS_2 structures as field-effect transistor channel arrays. ACS Nano. 2015;9:8773–8785. DOI: 10.1021/acsnano.5b01715

[72] Luo X, Lu X, Koon GKW, Neto AHC, Ozyilmaz B, Xiong QH, et al. Large frequency change with thickness in interlayer breathing mode-significant interlayer interactions in few layer black phosphorus. Nano Letters. 2015;15:3931–3938. DOI: 10.1021/acs.nanolett.5b00775

[73] Zhao Y, Luo X, Zhang J, Wu J, Bai X, Wang M, et al. Interlayer vibrational modes in few-quintuple-layer Bi_2Te_3 and Bi_2Se_3 two-dimensional crystals: Raman spectroscopy

and first-principles studies. Physical Review B. 2014;90:245428. DOI: 10.1103/PhysRevB.90.245428

[74] Lee G-H, Cui X, Kim YD, Arefe G, Zhang X, Lee C-H, et al. Highly Stable, dual-gated mos$_2$ transistors encapsulated by hexagonal boron nitride with gate-controllable contact, resistance, and threshold voltage. ACS Nano. 2015;9:7019–7026. DOI: 10.1021/acsnano.5b01341

[75] Roy T, Tosun M, Kang JS, Sachid AB, Desai SB, Hettick M, et al. Field-effect transistors built from all two-dimensional material components. ACS Nano. 2014;8:6259–6264. DOI: 10.1021/nn501723y

[76] Das S, Gulotty R, Sumant AV, Roelofs A. All two-dimensional, flexible, transparent, and thinnest thin film transistor. Nano Letters. 2014;14:2861–2866. DOI: 10.1021/nl5009037

[77] Dou X, Ding K, Jiang D, Sun B. Tuning and identification of interband transitions in monolayer and bilayer molybdenum disulfide using hydrostatic pressure. ACS Nano. 2014;8:7458–7464. DOI: 10.1021/nn502717d

[78] Wang Y, Cong C, Yang W, Shang J, Peimyoo N, Chen Y, et al. Strain-induced direct–indirect bandgap transition and phonon modulation in monolayer WS$_2$. Nano Research. 2015;8:2562–2572. DOI: 10.1007/s12274-015-0762-6

[79] Fu X-W, Liao Z-M, Zhou J-X, Zhou Y-B, Wu H-C, Zhang R, et al. Strain dependent resistance in chemical vapor deposition grown graphene. Applied Physics Letters. 2011;99:213107. DOI: 10.1063/1.3663969

[80] Bae S-H, Lee Y, Sharma BK, Lee H-J, Kim J-H, Ahn J-H. Graphene-based transparent strain sensor. Carbon. 2013;51:236–242. DOI: 10.1016/j.carbon.2012.08.048

[81] Zhu S-E, Ghatkesar MK, Zhang C, Janssen GCAM. Graphene based piezoresistive pressure sensor. Applied Physics Letters. 2013;102:161904. DOI: 10.1063/1.4802799

[82] Huang M, Pascal TA, Kim H, Goddard WA, III, Greer JR. Electronic-mechanical coupling in graphene from in situ nanoindentation experiments and multiscale atomistic simulations. Nano Letters. 2011;11:1241–1246. DOI: 10.1021/nl104227t

[83] He X, Gao L, Tang N, Duan J, Xu F, Wang X, et al. Shear strain induced modulation to the transport properties of graphene. Applied Physics Letters. 2014;105:083108. DOI: 10.1063/1.4894082

[84] Smith AD, Niklaus F, Paussa A, Vaziri S, Fischer AC, Sterner M, et al. Electromechanical piezoresistive sensing in suspended graphene membranes. Nano Letters. 2013;13:3237–3242. DOI: 10.1021/nl401352k

[85] Choi MK, Park I, Kim DC, Joh E, Park OK, Kim J, et al. Thermally controlled, patterned graphene transfer printing for transparent and wearable electronic/optoelectronic

system. Advanced Functional Materials. 2015;25:7109–7118. DOI: 10.1002/adfm. 201502956

[86] Zhao J, Wang G, Yang R, Lu X, Cheng M, He C, et al. Tunable piezoresistivity of nanographene films for strain sensing. ACS Nano. 2015;9:1622–1629. DOI: 10.1021/nn506341u

[87] Zhao J, He C, Yang R, Shi Z, Cheng M, Yang W, et al. Ultra-sensitive strain sensors based on piezoresistive nanographene films. Applied Physics Letters. 2012;101:063112. DOI: 10.1063/1.4742331

[88] Wang Y, Wang L, Yang T, Li X, Zang X, Zhu M, et al. Wearable and highly sensitive graphene strain sensors for human motion monitoring. Advanced Functional Materials. 2014;24:4666–4670. DOI: 10.1002/adfm.201400379

[89] Yang T, Wang Y, Li X, Zhang Y, Li X, Wang K, et al. Torsion sensors of high sensitivity and wide dynamic range based on a graphene woven structure. Nanoscale. 2014;6:13053–13059. DOI: 10.1039/c4nr03252g

[90] Ekinci KL, Roukes ML. Nanoelectromechanical systems. Review of Scientific Instruments. 2005;76:061101. DOI: 10.1063/1.1927327

[91] Chen C, Hone J. Graphene nanoelectromechanical systems. Proceedings of the IEEE. 2013;101:1766–1779. DOI: 10.1109/JPROC.2013.2253291

[92] Eichler A, Moser J, Chaste J, Zdrojek M, Wilson-Rae I, Bachtold A. Nonlinear damping in mechanical resonators made from carbon nanotubes and graphene. Nature Nanotechnology. 2011;6:339–342. DOI: 10.1038/nnano.2011.71

[93] Chen T, Mastropaolo E, Bunting A, Cheung R. Observation of second flexural mode enhancement in graphene resonators. Electronics Letters. 2015;51:1014–1016. DOI: 10.1049/el.2015.0361

[94] Grady E, Mastropaolo E, Chen T, Bunting A, Cheung R. Low frequency graphene resonators for acoustic sensing. Microelectronic Engineering. 2014;119:105–108. DOI: 10.1016/j.mee.2014.02.036

[95] Suk JW, Kirk K, Hao Y, Hall NA, Ruoff RS. Thermoacoustic sound generation from monolayer graphene for transparent and flexible sound sources. Advanced Materials. 2012;24:6342–6347. DOI: 10.1002/adma.201201782

AUTHOR QUERIES

AQ1	Kindly confirm the hierarchy level of section heading.
AQ2	Placeholder for Figuer 2, please do not alter
AQ3	Placeholder for fig. 3 Please, do not alter
AQ4	Placeholder for Table 1, please do not alter

| AQ5 | Placeholder for Table 2, please do not alter |